Multi-Channel Calibration for Airborne Post-Doppler Space-Time Adaptive Processing

André Barros Cardoso da Silva and Stefan V. Baumgartner
German Aerospace Center (DLR)
Microwaves and Radar Institute
82234 Wessling, Germany
Email: Andre.Silva@dlr.de

***Abstract*—This paper presents a fast and efficient multi-channel calibration algorithm for along-track systems, which in particular is evaluated for the post-Doppler space-time adaptive processing (PD STAP) technique. The calibration algorithm corrects the phase and magnitude offsets among the receiving channels, estimates and compensates the Doppler centroid variation caused by atmospheric turbulences by using the attitude angles of the antenna array. Important parameters and offsets are estimated directly from the radar range-compressed data. The proposed algorithm is compared with the state-of-the-art Digital Channel Balancing technique based on real multi-channel X-band data acquired by the DLR's airborne system F-SAR. The experimental results are shown and discussed in the frame of traffic monitoring applications.**

Keywords— Synthetic aperture radar (SAR), radar signal processing, radar applications, calibration, ground moving target indication (GMTI), airborne radar, traffic monitoring.

I. INTRODUCTION

Identical antennas and receiving channels cannot be built with the same electrical characteristics and time delays. As a result, the transfer functions and the antenna gain patterns of the receiving channels differ from each other and need to be characterized or equalized [1].

Generally, the transmitting (TX) and receiving (RX) antenna characteristics can be measured or estimated, the time delays between the RX channels can be compensated (e.g., by using external calibration), and remaining phase and magnitude offsets can be estimated from the data. In addition, the along-track baselines between the RX channels need to be precisely known in order to estimate the direction-of-arrival (DOA) angles of the targets accurately, which impact their position and velocity estimates.

The state-of-the-art technique known as Digital Channel Balancing (DCB) was introduced in [2] and discussed in detail in [1]. This technique performs an iterative approach in the two-dimensional frequency domain with the aim to balance the RX channels with respect to a reference channel. As a result, residual phase and magnitude offsets are corrected and the along-track baselines can be estimated accurately in the range-Doppler domain.

A detailed evaluation of different calibration techniques is presented in [3] for along-track interferometry (ATI), displaced phase center antenna (DPCA) and space-time adaptive processing (STAP) techniques. It is shown that the DCB is able to achieve the best clutter suppression performance among the other techniques, whereas at the expense of a higher computational effort.

In [4], an external calibration algorithm is presented for the new DLR's multi-channel digital-beamforming airborne system DBF-SAR [5]. The algorithm estimates accurately the antenna baselines and attitude angles, among other parameters. It is applied on range-compressed data (i.e., no azimuth compression is required) and relies on a previously measured antenna model for proper operation.

This paper presents a fast and efficient calibration algorithm for multi-channel airborne SAR systems that carries out: 1) correction of phase and magnitude offsets among the RX channels; and 2) Doppler centroid compensation along slant range and azimuth time by using the attitude angles of the antenna array. Important parameters and offsets are estimated from homogeneous range-compressed training data, stored in the memory and directly applied for the calibration of subsequent flights, which can speed up the overall processing time significantly.

II. POST-DOPPLER STAP OVERVIEW

In this paper, the post-Doppler (PD) STAP technique is used for ground moving target indication (GMTI). The PD STAP is able to perform clutter suppression as well as the moving target's detection and parameter estimation (e.g., Doppler frequency, line-of-sight velocity and DOA angle) [6]. The multi-channel signal model for the PD STAP can be expressed by [7]

$$\boldsymbol{s}(t) = \\ a_{\mathrm{s}} e^{-j\frac{4\pi}{\lambda}R(t)} D_{\mathrm{tx}}\left[u_{\mathrm{array}}(t)\right] \begin{bmatrix} D_{\mathrm{rx,1}}\left[u_{\mathrm{array}}(t)\right] e^{j\frac{2\pi}{\lambda}u_{\mathrm{array}}(t)x_1} \\ D_{\mathrm{rx,2}}\left[u_{\mathrm{array}}(t)\right] e^{j\frac{2\pi}{\lambda}u_{\mathrm{array}}(t)x_2} \\ \vdots \\ D_{\mathrm{rx,M}}\left[u_{\mathrm{array}}(t)\right] e^{j\frac{2\pi}{\lambda}u_{\mathrm{array}}(t)x_M} \end{bmatrix} \\ = a_{\mathrm{s}} e^{-j\frac{4\pi}{\lambda}R(t)} \boldsymbol{d}\left[u_{\mathrm{array}}(t)\right] \qquad (1)$$

where a_{s} is the reflectivity of the scatterer, λ is the radar wavelength, M is the number of RX channels, $R(t)$ is the range to the antenna array center, D_{tx} and $D_{\mathrm{rx,m}}$ are the complex TX and RX antenna characteristics of the m-th channel, x_m is the position of the antenna center in the azimuth (or flight) direction with respect to the antenna array center (cf. Fig. 1). The term $\boldsymbol{d}$ is known as DOA or beamforming vector, $u_{\mathrm{array}} = \cos(\Psi_{\mathrm{DOA,array}})$ is the directional cosine of the target and $\Psi_{\mathrm{DOA,array}}$ is the DOA angle of the target with respect to the antenna array axis.

Fig. 1 shows the acquisition geometry of a multi-channel antenna, for which the antenna array center origin is

978-1-7281-8942-0/20/$31.00 ©2020 IEEE

arbitrarily chosen at the center of the array. The DOA angle of the target measured with respect to the azimuth or flight direction is $\Psi_{\mathrm{DOA,az}}$. The antenna array and the azimuth axes coincide since the squint angle is assumed zero for simplicity, so that $\Psi_{\mathrm{DOA,array}} = \Psi_{\mathrm{DOA,az}}$.

The coordinates of the target are $\boldsymbol{x}_{\mathrm{t}} = [x_{\mathrm{t}}, y_{\mathrm{t}}, z_{\mathrm{t}}]^T$, where the symbol $[\cdot]^T$ terms the transpose operator, and the coordinates of the platform are $\boldsymbol{x}_{\mathrm{p}} = \left[x_{\mathrm{p}}, y_{\mathrm{p}}, z_{\mathrm{p}}\right]^T$.

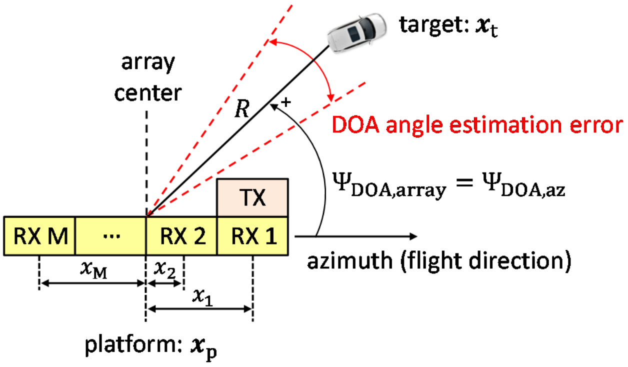

Fig. 1. Top view acquisition geometry with a multi-channel antenna. The squint angle is assumed zero for simplicity. In practice, channel imbalances may cause errors on the target's DOA angle estimation (in red).

The moving target detection is carried out by applying the following test statistics in range-Doppler domain [6]

$$\bar{T}(r_{\mathrm{k}}, f_{\mathrm{a}}) = \frac{\left|\boldsymbol{d}^H(u_{\mathrm{array}}, f_{\mathrm{a}}) \cdot \widehat{\boldsymbol{R}}_{\mathrm{W}}^{-1}(f_{\mathrm{a}}) \cdot \boldsymbol{z}(r_{\mathrm{k}}, f_{\mathrm{a}})\right|^2}{\boldsymbol{d}^H(u_{\mathrm{array}}, f_{\mathrm{a}}) \cdot \widehat{\boldsymbol{R}}_{\mathrm{W}}^{-1}(f_{\mathrm{a}}) \cdot \boldsymbol{d}(u_{\mathrm{array}}, f_{\mathrm{a}})} \lesseqgtr \eta \qquad (2)$$

where $[\cdot]^H$ is the Hermitian operator (complex conjugate transposition), f_{a} is the Doppler frequency, r_{k} is the range bin, η is the constant false alarm rate threshold (whose computation is carried out based on a clutter model [8]) and $\widehat{\boldsymbol{R}}_{\mathrm{W}}$ is the estimated clutter covariance matrix (CCM).

The CCM can be estimated empirically from homogeneous training data by applying the Sample Matrix Inverse technique according to [6]

$$\widehat{\boldsymbol{R}}_{\mathrm{W}}(f_{\mathrm{a}}) = \frac{1}{K} \sum_{k=1}^{K} \boldsymbol{z}(r_{\mathrm{k}}, f_{\mathrm{a}}) \cdot \boldsymbol{z}^H(r_{\mathrm{k}}, f_{\mathrm{a}}) \qquad (3)$$

where K range bins are used for averaging and $\boldsymbol{z}$ denotes the multi-channel data, which are generally composed of

$$\boldsymbol{z} = \boldsymbol{s} + \boldsymbol{c} + \boldsymbol{n} \qquad (4)$$

where $\boldsymbol{s}$ denotes the multi-channel moving target signal expressed in (1), $\boldsymbol{c}$ denotes the ground clutter and $\boldsymbol{n}$ denotes the uncorrelated background white noise.

The coordinates of the target in azimuth and in slant range can be expressed respectively as [6]

$$x_{\mathrm{t}} = x_{\mathrm{p}} + R \cdot \cos\left(\Psi_{\mathrm{DOA,az}}\right) \qquad (5)$$

$$y_{\mathrm{t}} = y_{\mathrm{p}} + R \cdot \sin\left(\Psi_{\mathrm{DOA,az}}\right) \qquad (6)$$

where the altitude of the target z_{t} can be obtained, for instance, from a digital elevation model.

Fig. 1 shows (in red) a potential estimation error of the target's DOA angle $\Psi_{\mathrm{DOA,az}}$, which in practice may be caused by channel imbalances that need to be estimated and corrected by a proper calibration algorithm (e.g., the algorithm presented in Section III). Note in (5) and (6) that the target's DOA angle $\Psi_{\mathrm{DOA,az}}$ impacts principally the estimation of the target's position.

III. CALIBRATION ALGORITHM

The simplified flowchart of the proposed algorithm is depicted in Fig. 2. The blue box shows the main steps for the channel imbalance correction (presented in detail in Section V), which is carried out adaptively and requires: the aircraft's navigation data (position, velocity, attitude angles and heading angle), the radar parameters and previously estimated parameters and offsets (cf. Section IV).

The Doppler centroid correction is important for the PD STAP technique in order to obtain an accurate CCM estimation (cf. (3)), which impacts the moving target's detection performance and parameter estimation accuracy.

The state-of-the-art DCB technique (which is compared with the proposed algorithm in Section VI) can be carried out alternatively for the phase and magnitude correction.

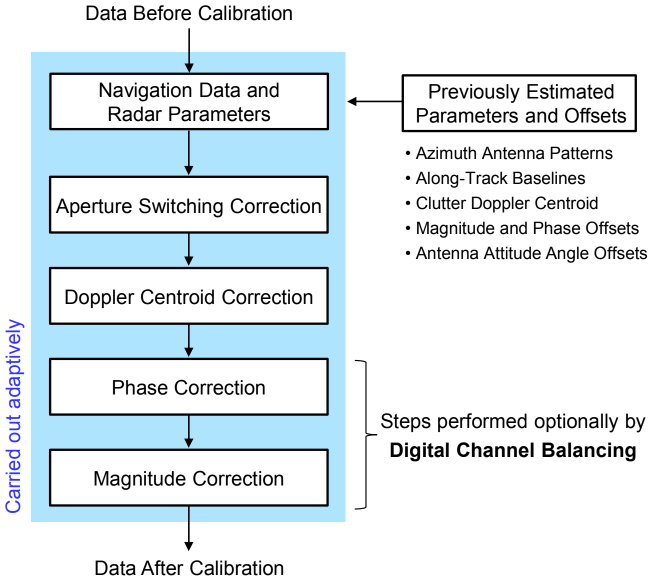

Fig. 2. Main steps of the proposed calibration algorithm.

IV. PARAMETER AND OFFSET ESTIMATION

A. Antenna Patterns

The envelope of the two-way diagram of the azimuth antenna pattern can be estimated from the radar data by

$$A_{\mathrm{m}}(f_{\mathrm{a}}, m) = \sqrt{\frac{1}{K} \sum_{k=1}^{K} |\boldsymbol{z}(r_{\mathrm{k}}, f_{\mathrm{a}}, m)|^2} \;, m = 1, \dots, M \qquad (7)$$

where m denotes the index of the RX channel and $\boldsymbol{z}$ denotes the multi-channel radar data expressed in (4).

B. *Magnitude Offsets*

The magnitude offsets can be obtained from the azimuth antenna pattern envelope maxima according to

$$\rho_{1,\mathrm{m}} = \frac{\max(A_1)}{\max(A_{\mathrm{m}})}, m = 2, \dots, M \qquad (8)$$

where the channel RX1 is assumed as reference.

C. *Along-Track Baselines*

The effective along-track baselines $d_{\mathrm{a}1,m}$ (which are half of the physical antenna center separations) are estimated from the radar data by using the slopes of the ATI phases $\phi_{1,\mathrm{m}}$ along the Doppler frequency f_{a} according to [1]

$$\phi_{1,\mathrm{m}}(f_{\mathrm{a}}) = -\frac{d_{\mathrm{a}1,\mathrm{m}}}{v_{\mathrm{p}}} \cdot f_{\mathrm{a}}, m = 2, \dots, M \qquad (9)$$

where the channel RX1 is assumed as reference.

D. *Clutter Doppler Centroid*

In practice, the aircraft is not able to follow a straight flight trajectory due to atmospheric turbulences, so that its attitude angles (yaw, pitch and roll) vary over time. The aircraft's motion plays an important role especially if the platform is equipped with a flat antenna array which does not allow zero-Doppler beam steering, as in the case of DLR's airborne system F-SAR [9]. The Doppler centroid variation can be expressed for a left-looking antenna as

$$f_{\mathrm{DC}}(r_{\mathrm{k}}, t) \approx \frac{2 \cdot v_{\mathrm{p}}}{\lambda}\Big[\cos\big(\theta_{\mathrm{i}}(r_{\mathrm{k}}) + \theta_{\mathrm{ROLL,ANT}}(t)\big) \tan\big(\theta_{\mathrm{PITCH,ANT}}(t)\big) + \sin\big(\theta_{\mathrm{i}}(r_{\mathrm{k}}) + \theta_{\mathrm{ROLL,ANT}}(t)\big) \cdot \tan\big(\theta_{\mathrm{YAW,ANT}}(t)\big)\Big] \qquad (10)$$

where θ_{i} is the incidence angle; $\theta_{\mathrm{YAW,ANT}}$, $\theta_{\mathrm{PITCH,ANT}}$ and $\theta_{\mathrm{ROLL,ANT}}$ are the yaw, pitch and roll angles of the antenna array, respectively. These angles can be expressed as

$$\theta_{\mathrm{YAW,ANT}}(t) = \theta_{\mathrm{YAW,IMU}}(t) + \Delta\theta_{\mathrm{YAW}} \qquad (11)$$

$$\theta_{\mathrm{PITCH,ANT}}(t) = \theta_{\mathrm{PITCH,IMU}}(t) + \Delta\theta_{\mathrm{PITCH}} \qquad (12)$$

$$\theta_{\mathrm{ROLL,ANT}}(t) = \theta_{\mathrm{ROLL,IMU}}(t) + \Delta\theta_{\mathrm{ROLL}} \qquad (13)$$

where $\theta_{\mathrm{YAW,IMU}}$, $\theta_{\mathrm{PITCH,IMU}}$ and $\theta_{\mathrm{ROLL,IMU}}$ are the yaw, pitch and roll angles of the aircraft, which are obtained from the inertial measurement unit (IMU) system.

The terms $\Delta\theta_{\mathrm{YAW}}$, $\Delta\theta_{\mathrm{PITCH}}$ and $\Delta\theta_{\mathrm{ROLL}}$ are the attitude angle offsets that can be estimated by the proposed calibration algorithm (cf. Section IV-E). The attitude angle offsets may arise due to an imperfect alignment of the antenna patches or elements, as well as due to the antenna pod's mounting on the aircraft's fuselage (i.e., non-parallel with respect to the aircraft's longitudinal axis).

For example, Fig. 3a shows a focused SAR image acquired by the DLR's airborne system F-SAR in the vicinity of Memmingen, in Germany. Fig. 3b shows the Doppler centroid variation estimated according to (10), which needs to be compensated by the calibration algorithm.

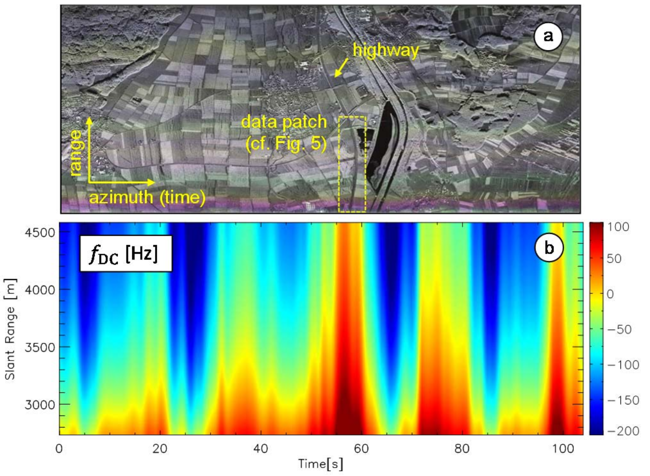

Fig. 3. (a) Focused SAR image acquired with DLR's airborne system F-SAR and (b) Doppler centroid estimated according to (10).

E. *Antenna Attitude Angle Offsets*

Two main steps are necessary for estimating the antenna attitude angle offsets ($\Delta\theta_{\mathrm{YAW}}$, $\Delta\theta_{\mathrm{PITCH}}$ and $\Delta\theta_{\mathrm{ROLL}}$):

1. A reference Doppler centroid of the scene $f_{\mathrm{DC,REF}}(r_{\mathrm{k}}, t)$ is estimated according to the reference channel RX1 (e.g., by using the energy balancing method proposed in [10]);

2. The antenna attitude angle offsets are obtained by means of multidimensional minimization (e.g., using the downhill simplex or Powell's method)

$$\underset{\overline{\Delta\theta}}{\operatorname{argmin}}\{\max(\|f_{\mathrm{DC,REF}}(r_{\mathrm{k}}, t) - f_{\mathrm{DC}}(r_{\mathrm{k}}, t, \overline{\Delta\theta})\|)\} \qquad (14)$$

where $f_{\mathrm{DC,REF}}(r_{\mathrm{k}}, t)$ is estimated from the radar data and $f_{\mathrm{DC}}(r_{\mathrm{k}}, t, \overline{\Delta\theta})$ is obtained from (10). The $\overline{\Delta\theta}$ dependency, denoted here explicitly, follows (11)-(13).

F. *Phase Offsets*

In practice, phase offsets can be introduced by the hardware of the radar system. The main steps needed for estimating the phase offsets from the radar data are:

1. Obtain the radar range-compressed data;

2. Select a data patch containing homogeneous clutter;

3. Estimate the phase offsets in time domain for each pair of RX channels according to [11]

$$\varphi_{1,m,\mathrm{offset}} = \arg\left(\frac{1}{N}\sum_{k=1}^{N} \boldsymbol{z}_1(k) \cdot \boldsymbol{z}_m^*(k)\right) \qquad (15)$$

where $\boldsymbol{z}_m^*$ is the complex conjugate and co-registered signal (with respect to RX1) and N is the total number of samples.

V. Channel Imbalance Correction

A. *Aperture Switching Correction*

The aperture switching (AS) technique can improve the GMTI performance of radar systems by creating additional phase centers and larger ATI baselines. Yet, this operation introduces a time delay that needs to be corrected. The correction can be carried out in Doppler frequency domain according to

$$\boldsymbol{z}_{\mathrm{AS,corr}}(r_{\mathrm{k}}, f_{\mathrm{a}}, m) = \boldsymbol{z}(r_{\mathrm{k}}, f_{\mathrm{a}}, m) \cdot \exp\left\{-j2\pi f_{\mathrm{a}} \Delta t_{\mathrm{AS}}\right\} \quad (16)$$

where $\boldsymbol{z}_{\mathrm{AS,corr}}$ is the radar data after the AS correction, $\Delta t_{\mathrm{AS}} = 1/(2 \cdot \mathrm{PRF})$ denotes the time lag introduced by the F-SAR antenna aperture switching and PRF is the pulse repetition frequency. It is pointed out that different AS schemes cause different time lags to be corrected [12].

B. *Doppler Centroid Correction*

The Doppler centroid can be corrected in time domain for each range bin and for each RX channel according to

$$\boldsymbol{z}_{\mathrm{FDC,corr}}(r_{\mathrm{k}}, t, m) = \boldsymbol{z}(r_{\mathrm{k}}, t, m) \cdot \exp\{-j2\pi t \Delta f_{\mathrm{DC}}(r_{\mathrm{k}})\} \quad (17)$$

where $\boldsymbol{z}_{\mathrm{FDC,corr}}$ is the radar data after Doppler centroid correction. The Doppler centroid variation along slant range Δf_{DC} can be obtained, for instance, for each coherent processing interval (CPI) according to

$$\Delta f_{\mathrm{DC}}(r_{\mathrm{k}}) = \frac{1}{n_{\mathrm{a,CPI}}} \sum_{t=0}^{n_{\mathrm{a,CPI}}-1} f_{\mathrm{DC}}(r_{\mathrm{k}}, t) \quad (18)$$

where $n_{\mathrm{a,CPI}}$ is the number of azimuth samples contained in a single CPI (e.g., $n_{\mathrm{a,CPI}} = 128$) and f_{DC} is estimated with (10) for the reference channel RX1. Thus, the range-dependent Doppler centroid is corrected for each CPI independently. Note that in (17) the same Doppler centroid $\Delta f_{\mathrm{DC}}(r_{\mathrm{k}})$ is applied to all RX channels.

C. *Phase Correction*

The phase correction with respect to channel RX1 can be carried out in time domain according to

$$\boldsymbol{z}_{\mathrm{ATI,corr}}(r_{\mathrm{k}}, t, m) = \boldsymbol{z}(r_{\mathrm{k}}, t, m) \cdot \exp\left\{j\Delta\hat{\varphi}_{1,m}(r_{\mathrm{k}}, t)\right\} \quad (19)$$

where $\boldsymbol{z}_{\mathrm{ATI,corr}}$ is the radar data after the phase correction and $\Delta\hat{\varphi}_{1,m}(r_{\mathrm{k}}, t)$ denotes the theoretical ATI phases estimated for each pair of RX channels according to

$$\Delta\hat{\varphi}_{1,m}(r_{\mathrm{k}}, t) = \frac{4\cdot\pi}{\lambda} \cdot \left[\frac{\lambda \cdot d_{\mathrm{a}1,m}}{2 \cdot v_{\mathrm{p}}} \cdot f_{\mathrm{DC}}(r_{\mathrm{k}}, t)\right] + \varphi_{1,m,\mathrm{offset}} \quad (20)$$

where the term $f_{\mathrm{DC}}(r_{\mathrm{k}}, t)$ is obtained with (10) and the offsets are the constants estimated beforehand (e.g., during the calibration flight).

D. *Magnitude Correction*

The magnitude offset correction with respect to channel RX1 can be carried out in time domain according to

$$\boldsymbol{z}_{\mathrm{mag,corr}}(r_{\mathrm{k}}, t, m) = \boldsymbol{z}(r_{\mathrm{k}}, t, m) \cdot \rho_{1,m} \quad (21)$$

where $\boldsymbol{z}_{\mathrm{mag,corr}}$ is the data after the magnitude correction and $\rho_{1,m}$ are the magnitude offsets estimated with (8).

VI. Experimental Results

The proposed algorithm is tested with real data acquired by DLR's airborne system F-SAR [9] and compared with the state-of-the-art DCB technique [2] in terms of processing time, phase correction accuracy and GMTI results.

A. *Processing Time*

This experiment compares the time required for:

1. Processing the blocks *Phase Correction* and *Magnitude Correction* (cf. Fig. 2) according to the mathematical framework presented in Section V-C and Section V-D;
2. Applying the established DCB technique [1], [2] that is used in many state-of-the-art GMTI algorithms for phase and magnitude correction (cf. Fig. 2).

For this time comparison, the data set shown in Fig. 3a was processed 1000 times for each of the previous two cases.

The proposed algorithm was about 15 times faster than the DCB since the phase correction is carried out with (15), where all terms are known or previously estimated (cf. Section IV). Absolute processing times are not considered here, since they severely depend on the employed computer architecture as well as the programming language.

The processing time reduction by a factor of 15 highlights the potential of the proposed algorithm towards real-time applications. Even so, for achieving real-time an efficient parallel implementation is required by taking into account potential multi-core and multi-processor architectures as well as graphical processing units.

B. *Phase Correction Accuracy*

Fig. 4 shows the histograms of interferometric phases obtained between the channels RX1 and RX2, before and after calibration, for the data set shown in Fig. 3a.

The histogram obtained before calibration (black) appears shifted by a phase offset ($\varphi_{1,2,\mathrm{offset}} = -103°$) and slightly skewed, which are typical effects of uncalibrated data [1]. In the histograms obtained after calibration using the proposed algorithm (blue) and the DCB (red), the phase distributions are centered around zero degrees, which indicates that the offset was compensated ($\varphi_{1,2,\mathrm{offset}} = 0°$). Note that the DCB (red) presents lower variance than the proposed algorithm (i.e., better phase correction accuracy).

Fig. 5 shows the ATI phases obtained from the data patch indicated in Fig. 3a, in which moving target signals can be clearly observed in the scale [-20° to 20°]. Note that more moving target signals are obtained with the proposed algorithm (Fig. 5a) in comparison with the DCB (Fig. 5b).

The reason is that the DCB is applied for each CPI independently and thus for CPIs containing several moving targets the DCB introduces some target self-whitening. Thus, less moving target signals are observed in Fig. 5b.

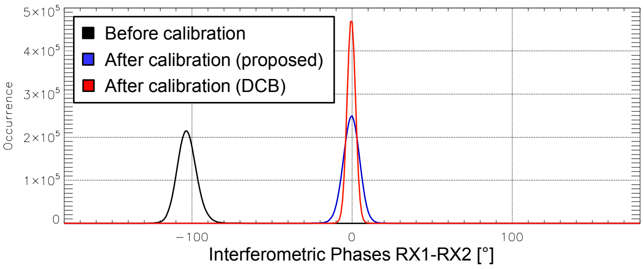

Fig. 4. Histograms of ATI phases (channels RX1-RX2) obtained from Fig. 3a: before (black) and after calibration using the proposed method (blue) and the DCB technique (red).

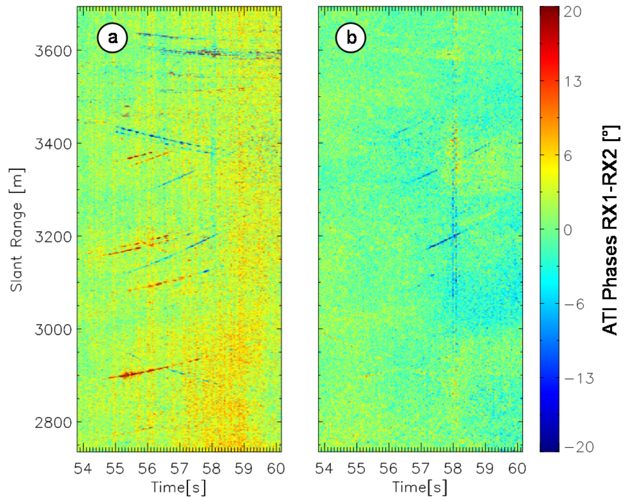

Fig. 5. ATI phases obtained from the data patch shown in Fig. 3a using: (a) the proposed method and (b) the DCB technique.

C. GMTI Results with Post-Doppler STAP

This experiment compares the proposed algorithm and the DCB in the frame of traffic monitoring with the PD STAP processor presented in [13]. Five controlled cars with different movements and speeds were considered (cf. the experiment description and the radar parameters in [14]).

Fig. 6 shows the GMTI results, in which Google Earth images are overlaid with radar detections (circles) obtained from the PD STAP processor. The detection colors are related to their absolute ground range velocities.

Fig. 6a shows the results obtained without calibration. In this case, none of the channel imbalances were corrected, which results in systematic phase errors and several false detections. Moreover, the cars are not detected and incorrect position and velocity estimates are obtained.

Fig. 6b and Fig. 6c show the much improved results obtained with the proposed algorithm and the DCB, respectively. In both cases, all cars are detected several times and a few false detections are obtained.

Table I summarizes for the results shown in Fig. 6b and Fig. 6c: the total number of radar detections (i.e., true and false detections), the number of true detections and the probability of false alarm $\hat{P}_{\mathrm{fa}}$, which is estimated from the radar data according to

$$\hat{P}_{\mathrm{fa}} = \frac{\mathrm{All}-\mathrm{True}_{\#1-5}}{n_{\mathrm{a}}\cdot n_{\mathrm{r}}} \qquad (22)$$

where $n_{\mathrm{a}} = 16384$ is the number of azimuth samples and $n_{\mathrm{r}} = 1024$ is the number of range bins of data set [14].

The number of true detections of cars 1 to 5 (True#1-5) can be counted since the exact geographical positions and velocities of such controlled cars are known [13]. The other detections that lie far from the roads with different velocities are considered as false.

Table I shows that the proposed algorithm obtains more true detections. On the other hand, the DCB obtains lower $\hat{P}_{\mathrm{fa}}$ (i.e., less false detections). For traffic monitoring, the problem of false detections can be circumvented with our PD STAP processor with a priori knowledge information [13] which rejects most of the false detections that lie far from the roads.

Fig. 7 shows the velocity estimates of the true detections obtained with the proposed algorithm and the DCB, which were similar and accurate according to the ground truth [14].

Further details and results obtained with the proposed calibration algorithm can be found in [15].

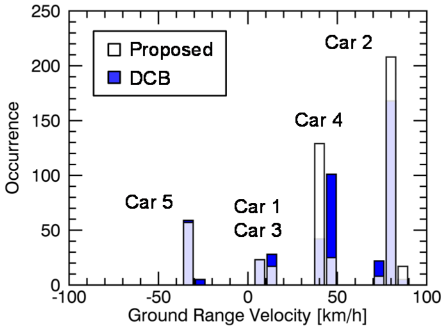

Fig. 7. Ground range velocity histograms of the true detections obtained with the proposed algorithm (white bars) and the DCB (blue bars).

TABLE I. QUANTITATIVE COMPARISON BETWEEN THE PROPOSED ALGORITHM AND THE DCB (CF. FIG. 6B AND FIG. 6C).

Algorithm	**All**	**True (#1-5)**	$\hat{P}_{fa}$ [x10^{-6}]
Proposed	661	484	10.55
DCB	575	453	7.27

VII. CONCLUSION

The experimental results show that the proposed method is about 15 times faster than the state-of-the-art DCB and obtains more true detections (in the frame of traffic monitoring) due to its robustness against target self-whitening. Nevertheless, the DCB achieves better phase correction accuracy due to its superior clutter suppression capability, which results in a reduced number of false detections.

The proposed algorithm presents also potential use in the frame of maritime applications, for which it is foreseen that the required parameters and offsets are estimated at the beginning of the flight campaign using homogeneous land clutter. In this sense, future experiments on ship detection are foreseen with the new DLR's multi-channel digital-beamforming airborne system DBF-SAR [5].

REFERENCES

[1] C. H. Gierull, “Digital Channel Balancing of Along-Track Interferometric SAR Data,” Ottawa, Canada, 2003.

[2] J. H. G. Ender, “The Airborne Experimental Multi-Channel SAR-System AER-II,” in *European Conference on Synthetic Aperture Radar (EUSAR)*, 1996, pp. 49–52.

[3] A. Bertetich, “Investigation of Multi-Channel SAR Calibration Methods for Real-Time Traffic Monitoring,” Opera Universitaria di Trento, 2010.

[4] M. Jaeger, R. Scheiber, and A. Reigber, “Robust , Model-Based External Calibration of Multi-Channel Airborne SAR Sensors Using Range Compressed Raw Data,” *Remote Sens.*, vol. 11, no. 22, p. 28, 2019.

[5] A. Reigber *et al.*, “First Interferometric Trials with the Airborne Digital-Beamforming DBFSAR System,” in *European Conference on Synthetic Aperture Radar (EUSAR)*, 2018, pp. 12–15.

[6] W. L. Melvin, “A STAP overview,” *IEEE Aerosp. Electron. Syst. Mag.*, vol. 19, no. 1, pp. 19–35, 2004.

[7] J. H. G. Ender, C. H. Gierull, and D. Cerutti-Maori, “Improved space-based moving target indication via alternate transmission and receiver switching,” *IEEE Trans. Geosci. Remote Sens.*, vol. 46, no. 12, pp. 3960–3974, 2008.

[8] C. H. Gierull, “Statistical analysis of multilook SAR interferograms for CFAR detection of ground moving targets,” *IEEE Trans. Geosci. Remote Sens.*, vol. 42, no. 4, pp. 691–701, 2004.

[9] A. Reigber *et al.*, “Very-high-resolution airborne synthetic aperture radar imaging: signal processing and applications,” *Proc. IEEE*, vol. 101, no. 3, pp. 759–783, 2013.

[10] R. Bamler, “Doppler Frequency Estimation and the Cramér-Rao Bound,” *IEEE Trans. Geosci. Remote Sens.*, vol. 29, no. 3, pp. 385–390, 1991.

[11] C. H. Gierull, “Moving Target Detection with Along-Track SAR Interferometry,” Ottawa, Canada, 2002.

[12] D. Cerutti-Maori, C. H. Gierull, and J. H. G. Ender, “Experimental verification of SAR-GMTI improvement through antenna switching,” *IEEE Trans. Geosci. Remote Sens.*, vol. 48, no. 4 PART 2, pp. 2066–2075, 2010.

[13] A. B. C. Silva and S. V. Baumgartner, “Novel post-Doppler STAP with a priori knowledge information for traffic monitoring applications : basic idea and first results,” *Adavances Radio Sci.*, vol. 15, pp. 77–82, 2017.

[14] S. V. Baumgartner and G. Krieger, “Fast GMTI algorithm for traffic monitoring based on a priori knowledge,” *IEEE Trans. Geosci. Remote Sens.*, vol. 50, no. 11, pp. 4626–4641, 2012.

[15] A. B. C. Silva, S. V. Baumgartner, F. Q. Almeida, and G. Krieger, “In-Flight Multi-Channel Calibration for Along- Track Interferometric Airborne Radar,” *IEEE Trans. Geosci. Remote Sens.*, pp. 1–18, 2020 (accepted).

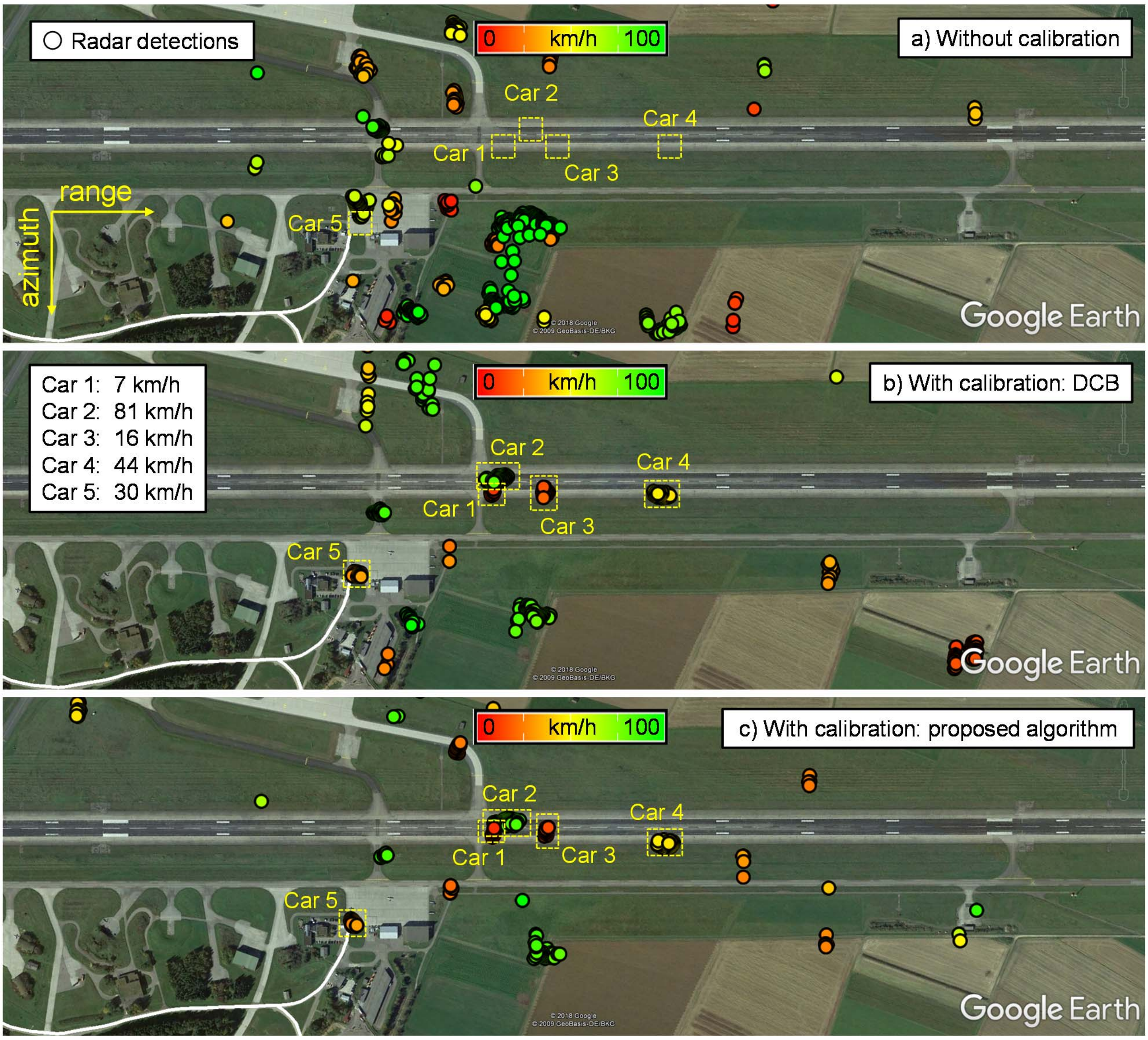

Fig. 6. GMTI results obtained in the region of the Memmingen’s Allgäu airport, in Germany. The Google Earth images are overlaid with radar detections (circles) obtained from real four-channel X-band data acquired with F-SAR: (a) without calibration, (b) with calibration using the state-of-the-art DCB technique and (c) with calibration using the proposed algorithm. The ground velocities of the cars are shown according to the ground truth in [14].